



# CHORUS

This is the accepted manuscript made available via CHORUS. The article has been published as:

## Role of nonlinearities in topological protection: Testing magnetically coupled fidget spinners

Javier Vila, Glaucio H. Paulino, and Massimo Ruzzene

Phys. Rev. B **99**, 125116 — Published 12 March 2019

DOI: [10.1103/PhysRevB.99.125116](https://doi.org/10.1103/PhysRevB.99.125116)

1           **The role of nonlinearities in topological protection: using**  
2                           **magnetically coupled fidget spinners**

3                           Javier Vila<sup>1,2</sup>, Glaucio H. Paulino<sup>1</sup>, Massimo Ruzzene<sup>2,3\*</sup>

4           <sup>1</sup> *School of Civil Engineering, Georgia Institute of Technology, Atlanta GA 30332*

5 <sup>2</sup> *School of Aerospace Engineering, Georgia Institute of Technology, Atlanta GA 30332 and*

6                           <sup>3</sup> *School of Mechanical Engineering,*

7                           *Georgia Institute of Technology, Atlanta GA 30332*

8                           (Dated: February 7, 2019)

                          Abstract

We investigate and experimentally observe the existence of topologically protected interface modes in a one-dimensional mechanical lattice, and we report on the effect of nonlinearities on topological protection. The lattice consists of a one-dimensional array of spinners with nearest neighbor coupling resulting from magnetic interactions. The distance between the spinners is spatially modulated to obtain a diatomic configuration, and to produce a non-trivial interface by breaking spatial inversion symmetry. For small amplitudes of motion, the interactions are approximately linear, and the system supports topologically protected interface modes at frequencies inside the bulk bandgap of the lattice. Nonlinearities induced by increasing amplitude of motion cause the interface modes to shift and merge with the bulk bands. The resulting edge-to-bulk transition causes the extinction of the topologically protected interface mode and extends it to the entire length of the chain. Such transition is predicted by analytical calculations and verified by experimental observations. The paper thus investigates topologically protected interface modes obtained through broken spatial inversion symmetry, and documents the lack of robustness in the presence of nonlinearities.

## 9 I. INTRODUCTION

10 Notable efforts have been devoted to the investigation of topological protection in con-  
11 densed matter<sup>1,2</sup>, and in classical areas of wave physics such as acoustics<sup>3</sup>, photonics<sup>4,5</sup>, as  
12 well as solid<sup>6,7</sup> and fluid mechanics<sup>8</sup>. The phenomenon of topological protection consists in  
13 the existence of wave modes that do not propagate into the bulk of the considered media,  
14 but are instead confined to a lower dimensional region within it, either a boundary or an  
15 interface. Driven by its topological nature, this effect is robust to the existence of imper-  
16 fections and defects, making it attractive for applications where lossless wave propagation,  
17 immunity to backscattering and mode localization are important objectives. Topological  
18 protection can be achieved through *time-reversal symmetry* breaking, which generally re-  
19 quires the employment of active elements that effectively bias the interactions within the  
20 media. Examples include circulators in optomechanics<sup>9</sup>, gyroscopic mechanical metamateri-  
21 als<sup>10</sup>, and the use of active fluids characterized by a background flow<sup>11</sup> among others. These  
22 systems mimic the quantum Hall effect whereby a net “magnetic” flow breaks time-reversal  
23 symmetry. Two superimposing effects lead to the emergence of topologically protected (TP)  
24 modes. First, bandgaps are opened at the otherwise high symmetry degeneracy points in  
25 reciprocal space (e.g. Dirac cones). Second, the integral of the Berry curvature of each  
26 band along the reciprocal space does not equal zero, and the separated dispersion surfaces  
27 are linked only by one lower dimensional band, which corresponds to the TP mode. The  
28 eigenvector associated with this band is localized to a lower dimensional region in space and  
29 propagation is unidirectional<sup>12</sup>. Similar effects are achieved through solely passive elements  
30 that break *spatial inversion symmetry* (SIS)<sup>13,14</sup>. Spatial inversion symmetry breaking also  
31 opens bandgaps at the high symmetry points and couples the spins (or polarities) of other-  
32 wise degenerate modes. In this case, the integral of the Berry curvature is nonzero in the  
33 vicinity of the opened Dirac cone, although it is zero over the entire reciprocal space. Two  
34 lower dimensional bands are produced and are associated with TP modes localized at the  
35 interface of two lattices with inverted bands, i.e. bands that are characterized by oppo-  
36 site values of the relevant topological invariants, and propagation of these associated modes  
37 occurs in opposite directions<sup>7</sup>.

38 In systems that involve active elements, topological protection may be tailored or removed  
39 by control of such elements. In passive systems, the control of TP modes must instead rely on  
40 the inherent dynamic behavior of the lattice. Thus, nonlinearities appear as natural choices  
41 to pursue the objective of controlling and tailoring TP modes. Indeed, the vast majority  
42 of studies in the field of topological protection is limited to linear systems. While some  
43 theoretical investigations involving topological transitions have been recently presented<sup>15,16</sup>,  
44 the physical demonstration of how nonlinearities affect TP modes remains mostly unexplored.  
45 Nonlinearities, for example, enable uneven distributions of the wave energy, which in turn  
46 may lead to nonreciprocal wave propagation<sup>17-21</sup>. Another interesting nonlinear effect is the  
47 change in the effective parameters governing wave motion, such as the equivalent stiffness of  
48 elastic systems, which produces shifts of dispersion branches and bandgaps<sup>22,23</sup>.

49 The theoretical analysis of nonlinearities and their effect on a topologically non-trivial  
50 interface is presented in<sup>16</sup>, where results suggest lack of robustness of TP modes obtained  
51 through SIS breaking in the presence of a nonlinear interface. The present work sets the  
52 objective of observing this behavior experimentally. To this end, a nonlinear lattice con-  
53 sisting of units that interact through permanent magnets is modeled, assembled and then  
54 tested. Magnetic interactions provide the means for modulating the strength of the lat-  
55 tice coupling through proper adjustment of the interatomic spacing, and naturally intro-  
56 duce nonlinearities as the amplitude of wave motion increases. Topological protection is  
57 induced and subsequently verified via SIS breaking at a selected location, and is shown to  
58 undergo an interface-to-bulk transition for increasing amplitude. This occurs solely as a re-  
59 sult of amplitude-dependent stiffness softening of the magnetic interaction, without requiring  
60 changes in the system's physical topology.

61 Following this introduction (Sec. I), Sec. II is devoted to the description of the considered  
62 lattice, its main physical parameters and the study of its corresponding analytical model,  
63 both in linear and nonlinear regimes. The experimental investigations are described in  
64 Sec. III. Finally, Sec. IV summarizes the key findings of the study and highlights potential  
65 extensions. Three Appendices supplement the work.

## 66 II. LATTICE CONFIGURATION AND ANALYTICAL RESULTS

67 The investigations on TP and nonlinearities presented in<sup>16</sup> have shown that localized  
68 modes arise at the interface between two spring-mass chains that are inverted copies of each  
69 other. In the presence of nonlinearities, amplitude-dependent frequency shifts cause the  
70 localized TP mode to migrate to the bulk spectrum. This behavior is further investigated in  
71 this paper through the physical implementation of a 1D lattice consisting of a dimer chain  
72 of spinners<sup>24</sup>, see Fig. 1. Each spinner is bolted to a linear guide, which fixes its position  
73 while letting it free to rotate about an axis perpendicular to the page. The spinners are  
74 coupled through permanent magnets in attraction that provide a force that tends to maintain  
75 the spinners in the aligned position (Fig. 1(a)). The magnitude of magnetic interactions is  
76 strongly related to the distance between the magnets, which is defined by the spacing between  
77 the spinners. Such spacing is here modulated to implement a dimer lattice configuration  
78 whereby the interaction coefficients are defined by two distance values, namely  $D_a$  and  $D_b$   
79 (Fig. 1). An interface is created by joining the lattice with its mirror copy at a defined  
80 location as a result of broken SIS (Fig. 1(b)).

### 81 A. Analytical model

82 A simplified model is formulated according to the configuration of Fig. 2. The dynamic  
83 behavior of each spinner is described by its rotation angle  $\theta$ , and governed by the spinner  
84 inertia  $I$  and by the interaction with its neighbors. Such interaction is evaluated based  
85 on the model of the magnetic force exchanged by the permanent magnets mounted on the  
86 spinner's pegs, which can be approximated to varying orders in terms of the angular positions  
87 of the spinners. Details of the evaluation of the magnetic interactions and their simplified  
88 description can be found in Appendix A.

89 According to the approximations made and the derivations reported in the Appendix A,  
90 the equations of motion for the  $i$ -th unit cell can be expressed as follows:

$$\begin{aligned}
I\ddot{\theta}_{a,i} + k_\theta\theta_{a,i} + k_{t,a}(\theta_{b,i} + \theta_{a,i}) + k_{t,b}(\theta_{a,i} + \theta_{b,i-1}) + \gamma_a(\theta_{b,i} + \theta_{a,i})^3 + \gamma_b(\theta_{a,i} + \theta_{b,i-1})^3 &= 0 \\
I\ddot{\theta}_{b,i} + k_\theta\theta_{b,i} + k_{t,b}(\theta_{a,i+1} + \theta_{b,i}) + k_{t,a}(\theta_{b,i} + \theta_{a,i}) + \gamma_b(\theta_{a,i+1} + \theta_{b,i})^3 + \gamma_a(\theta_{b,i} + \theta_{a,i})^3 &= 0
\end{aligned}
\tag{1}$$

<sup>91</sup> where  $I$  is the inertia of each spinner,  $k_{\theta_a}, k_{\theta_b}, k_{t_a}, k_{t_b}$  are the linear interaction coefficients,  
<sup>92</sup> while  $\gamma_a, \gamma_b$  define the nonlinear interaction coefficients. The equations for the inverted unit  
<sup>93</sup> cell are formally identical, with the proper switching of the subscripts, and are reported in  
<sup>94</sup> Appendix A for brevity.

<sup>95</sup> Analysis of the equations reveals that the motion of each spinner is governed by its rotary  
<sup>96</sup> inertia, and by the magnetic interactions that in the linear regime manifest themselves  
<sup>97</sup> as a term that is proportional to the rotation of each individual spinner. This effectively  
<sup>98</sup> produces the effect of a torsional spring connected to the ground. An additional term couples  
<sup>99</sup> neighboring spinners through a torque that is approximately proportional to the relative  
<sup>100</sup> displacement between neighboring magnets in the direction transverse to the spinners chain,  
<sup>101</sup> here measured by the sum of their respective rotation angles. **The presence of the ground**  
<sup>102</sup> **term, and the fact that nearest neighbor interactions are defined by the sum of the rotation**  
<sup>103</sup> **angles, instead of their difference, make the system slightly different than a typical dimer**  
<sup>104</sup> **chain of the kind investigated for example in<sup>16</sup>.**

## <sup>105</sup> B. Linear dispersion analysis and associated topology

<sup>106</sup> We first investigate the underlying linear behavior of the lattice, by considering small  
<sup>107</sup> angular perturbations and neglecting the nonlinear terms in Eq. (1). We evaluate the dis-  
<sup>108</sup> persion properties for the infinite lattice by imposing a plane wave solution in the form  
<sup>109</sup>  $\theta_{p,i} = \theta_{p,0}e^{j(i\mu - \omega t)}$ , where  $i$  is an integer defining the location of the unit cell,  $p = a, b$ ,  
<sup>110</sup>  $j = \sqrt{-1}$ , while  $\omega$  denotes the angular frequency and  $\mu$  the dimensionless wavenumber. Sub-  
<sup>111</sup> stituting these expressions in Eqs. (1), we obtain an eigenvalue problem that identifies the

112 following two dispersion branches:

$$\omega^2 = \frac{1}{I} (k_\theta + k_{t,a} + k_{t,b}) \pm \frac{1}{I} \sqrt{k_{t,a}^2 + k_{t,b}^2 + 2k_{t,a}k_{t,b} \cos \mu}, \quad (2)$$

113 The branches are separated by one bandgap (shaded blue area in Fig. 3(a)). In addi-  
 114 tion, a zero-frequency gap extending up to a cut-off is produced by the grounding constants  
 115  $k_\theta$ . Breaking of spatial inversion symmetry by inverting the order of the distance modula-  
 116 tions, produces dispersion curves that differ in terms of the associated topological invariants.  
 117 Specifically, the topological properties of the second and third bandgaps can be switched by  
 118 permutation of the intra-cell and inter-cell connecting springs, i.e. inverting the unit cell, or  
 119 by considering  $k_{t,a} > k_{t,b}$  or vice versa, i.e.  $k_{t,b} > k_{t,a}$ . The topological invariant, the Zak  
 120 phase<sup>25</sup> in the case of a 1D lattice, is evaluated through numerical integration of the eigen-  
 121 vector change along each band as described in<sup>16,26,27</sup>. It is found that the Zak phase is  $\mathcal{Z} = \pi$   
 122 for both dispersion bands when  $k_{t,a} < k_{t,b}$ , while it is  $\mathcal{Z} = 0$  otherwise. Hence, the interface  
 123 of Fig.1(b) connects two lattices with same bandgap, but inverted geometry and different  
 124 band topology. Thus, the interface supports modes whose frequency can be predicted from  
 125 the solution of the eigenvalue problem for a finite system. The eigenvalues obtained for two  
 126 reversed lattices with 20 spinners each confirm the existence of the two branches separated  
 127 by the gap, along with the presence of two additional modes (black and green solid dots),  
 128 one of which appears inside the bandgap (black solid dot). Both modes are localized at the  
 129 interface as illustrated by the corresponding eigenvectors shown in Fig. 3(c). The two inter-  
 130 face modes are characterized by distinct spatial profiles, whereby the lower frequency mode  
 131 is odd relative to the interface, while the higher frequency mode is symmetric, or even, with  
 132 respect to it. Of interest is the mode in the bandgap, which is topologically protected (TP)  
 133 as a result of broken SIS and according to Zak phase computations presented in<sup>16</sup>. This TP  
 134 mode is the focus of the investigations in the remainder of the paper.

135 **C. Effects of nonlinear interactions**

136 We evaluate the effect of increasing amplitude on the eigenvalues and associated eigen-  
 137 modes of the system. To this end, we consider the governing equations for the finite  
 138  $N + N = 40$  system with interface, which are obtained from the assembly of equations  
 139 in Eq. (1). Assuming harmonic motion  $\theta_n e^{j\omega t}$  and applying harmonic balance, we obtain the  
 140 general matrix form:

$$\mathbf{K}(\boldsymbol{\theta})\boldsymbol{\theta} = \omega^2 I \boldsymbol{\theta}. \quad (3)$$

141 where  $\boldsymbol{\theta} = [\theta_{a,1}, \theta_{b,1}, \dots, \theta_{a,N}, \theta_{b,N}]^T$  is a vector including the complex amplitudes of all angular  
 142 degrees of freedom of the lattice,  $\mathbf{K}(\boldsymbol{\theta})$  denotes the effective stiffness matrix and  $\boldsymbol{\theta} e^{j\omega t}$ .  
 143 For low amplitudes  $|\boldsymbol{\theta}| \ll 1$ , the stiffness matrix  $\mathbf{K}$  is independent of  $\boldsymbol{\theta}$  and the solution  
 144 is straightforward. However, when nonlinearities play a role the effective stiffness matrix  
 145 depends on the amplitudes of motion, which requires an iterative analysis. Specifically, we  
 146 use a Newton-Raphson scheme<sup>28</sup>.

147 To write the nonlinear governing equations in canonical form, Eq. (3) is rearranged as:

$$[\mathbf{K}(\boldsymbol{\theta}) - \omega^2 I] \boldsymbol{\theta} = 0. \quad (4)$$

148 This system of  $2N$  equations has  $2N + 1$  unknown variables  $\{\boldsymbol{\theta}, \omega\}$ , and therefore infinite  
 149 solutions. To extract specific  $\{\boldsymbol{\theta}, \omega\}$  pairs, we impose particular values to the total amplitude  
 150 of the chain  $A$ , defined as the  $L_2$  norm of  $\boldsymbol{\theta}$ . Thus we add the additional equation  $|\boldsymbol{\theta}|_2 - A = 0$ ,  
 151 where  $A$  has a numeric value. When  $A \rightarrow 0$  is imposed, the linear solution is recovered.

152 We start by solving for a small value of  $A$  (e.g.  $A = 10^{-3}$ ), and we use the linear  
 153 eigenvector-eigenvalue pair  $\{\boldsymbol{\theta}_l, \omega_l\}$  as initial guess. The linear eigenvector  $\boldsymbol{\theta}_l$  is simply scaled  
 154 as  $\boldsymbol{\theta}_g = \boldsymbol{\theta}_l / |\boldsymbol{\theta}_l|_2 A$  and the linear eigenvalue  $\omega_l$  is used as is. This way we ensure that the initial  
 155 guess  $\boldsymbol{\theta}_g$  is the eigenvector of the linear problem and that its total amplitude  $|\boldsymbol{\theta}_g|$  is  $A$ . The  
 156 algorithm yields a new solution that is then used as the initial guess for a slightly higher value  
 157 of  $A$ , and so on. With this procedure we calculate the evolution of the eigenvalue-eigenvector  
 158 pair for increasing values of total amplitude  $A$ .

159 Depicted in Figs. 4(a)-(d) are results for the TP mode for the values of  $\gamma_{a(b)} = -366(-188)$   
 160  $\text{Nm/rad}^3$  (see Appendix B1). Results show that the nonlinear “eigen-frequency” decreases

161 with amplitude, along with an amplitude-dependent transition whereby the frequency exits  
 162 the bandgap (shaded blue area in Fig. 4.a) and enters the bulk spectrum of the linear system.  
 163 This is consistent with the negative value of  $\gamma_{a(b)}$  that defines a softening nonlinearity in the  
 164 connecting springs, by which their effective stiffness decreases for increasing total amplitude  
 165  $A$ . When the nonlinear eigenvalue abandons the bandgap, the bulk attenuation of this  
 166 otherwise localized wave mode no longer holds, and the wave mode extends to the bulk.  
 167 This is illustrated in Fig. 4(b), which presents the variation of the corresponding eigenvector  
 168 for increasing amplitude  $A$ . In the figure, the colors are associated with the magnitude of each  
 169 mode normalized to its maximum value, i.e.  $\theta(A)/|\theta(A)|_\infty$ . Also, the markers correspond  
 170 to the normalized angular motion of the individual spinner, while the continuous solid lines  
 171 are spline interpolations that improve visualization.

172 Both plots in Fig. 4(a),(b) illustrate the occurrence of an interface-to-bulk transition as  
 173 the amplitude of wave motion increases, and show the importance of nonlinearities. The  
 174 transition is denoted by the thick, solid red lines in both figures at  $A \approx 0.09$  rad and is  
 175 further illustrated in Fig. 4(c), which compares the magnitude of the eigenvector at spinner  
 176  $n = 22$  close to the interface (solid blue line), and away from the interface at  $n = 1$  (dashed  
 177 green line). For low amplitudes, motion at  $n = 1$  is very limited, and negligible compared to  
 178 the motion at the interface  $n = 22$ . As amplitude grows, there is an evident increase in the  
 179 motion at  $n = 1$  as a result of the mode becoming global in nature and no longer localized  
 180 at the interface. A thick red line at  $A \approx 0.09$  rad is added to the plot for reference purposes.

### 181 III. EXPERIMENTS

182 We experimentally evaluate the existence of TP mode and the influence of amplitude  
 183 and associated nonlinearities through the 40 spinner array shown in Fig. 5. The spinners are  
 184 bolted to a longitudinal aluminum beam at distances  $D_a$  and  $D_b$ . The magnets employed are  
 185 bonded to the pegs of the spinners, with aligned magnetization vectors poled in attraction.  
 186 The method used to experimentally characterize the magnetic interaction as a function of  
 187 the distance between the magnets is described in Appendix B. The key model parameters  
 188 identified through the experiments are listed in Table B.1. Additional details of geometric

189 properties of the magnets, spinners and the chain are provided in Appendix C.

190 In the experiments, excitation is provided by an electrodynamic shaker controlled by a  
191 signal generator that provides the desired input. Specifically the signals used in the exper-  
192 iments are a white noise signal band-limited to the frequency range of interest (0 – 80 Hz)  
193 and a sine wave at the target frequency and amplitude. The response of the spinner array  
194 is recorded by a single point Laser Doppler vibrometer (LDV) pointed at selected locations.  
195 Experiments are conducted for excitation applied at spinner  $n = 1$  at the left boundary of the  
196 array, and at spinner  $n = 20$  close to the interface (Fig. 5). The first configuration evaluates  
197 the transmissibility through the array, while the excitation right at the interface ( $n = 22$ )  
198 directly probes the TP modes and investigates changes as a function of amplitude. Video  
199 recordings of the response of the spinner arrays are also taken through a high speed camera,  
200 the results of which are processed to provide the spatial distribution of the response and show  
201 mode localization and to produce the animations presented as part of the Supplementary  
202 Material (SM)<sup>29</sup>. In the SM videos, we show the spinners chain oscillating at the nonlinear  
203 normal frequencies of three different values of the amplitude denoted as low  $A = 0.002$  rad,  
204 medium  $A = 0.070$  rad and high  $A = 0.179$  rad. We superimpose a circle on top of every  
205 spinner whose radius is proportional to the spinner amplitude of motion  $|\Theta_n|$  for improved  
206 visualization. The interiors of these circles are colored to indicate the instantaneous phase of  
207 each spinner measured as the argument of the complex number  $\theta_n e^{j\omega t}$  in absolute value, go-  
208 ing from cyan to magenta from lowest to highest value of the spinner oscillation magnitude.  
209 A small oscillating white circle is also attached to the perimeter of each circle to further  
210 highlight the angular motion. For verification of the LDV measurements, one point of each  
211 spinner, located next to the one of the magnets, is tracked to extract the spinner motion  $\theta_n$   
212 from the videos. The points are marked in the animations with a blue dot surrounded by a  
213 red square. We track the motion by comparing the relative position of the pixel set inside  
214 the red square among subsequent frames.

215 As in the analytical investigations, we first probe the linear behavior of the system by  
216 evaluating its dynamic behavior at low amplitude. To this end, we measure the frequency  
217 response at  $n = 22$  for white noise excitation applied at spinner  $n = 1$  during 20 seconds, and  
218 averaged for 150 repetitions. The results are presented in Fig. 6 (black solid line). For ref-

219 erence the figure also reports the corresponding analytical predictions (red solid line), along  
220 with the predicted eigenvalues (red circles), and the frequency bandgaps (shaded beige, cyan  
221 and purple regions). The results show a good match between analytical and experimental  
222 results, and confirm the overall behavior of the system, including the existence of bandgaps  
223 and of the two interface modes, both highlighted in the figure, one being the TP mode of  
224 interest.

225 We investigate amplitude effects around the frequency of the TP mode by imposing  
226 harmonic motion at  $n = 20$  and record the applied force through a load cell mounted on the  
227 stinger connected to the shaker, and the velocity of spinner  $n = 22$ . All results presented  
228 herein are at steady-state for frequency varying between 35 Hz and 55 Hz, and amplitude of  
229 imposed motion  $\theta_{20}e^{j\omega t}$  increasing approximately between  $|\theta_{20}| = 0.001$  rad and  $|\theta_{20}| = 0.07$   
230 rad. Since the shaker is controlled in open-loop, we control the amplitude of the electronic  
231 signal that excites it, and  $\theta_{20}$  is evaluated as the magnitude of the motion of spinner  $n = 20$ ,  
232 recorded by an accelerometer. The amplitude  $\theta_{22}$  of spinner  $n = 22$  is also calculated as the  
233 first harmonic of its motion  $\theta_{22}$ , measured with the LDV. The amplitude of applied force  
234  $f_0$  is calculated as the first harmonic of the instantaneous force measured by the load cell.  
235 Second and higher harmonics of all the measurements have been found more than an order  
236 of magnitude lower than the first harmonic.

237 Each experiment produces a triplet of values: the amplitude of the response  $\theta_{22}$ , its  
238 frequency, and the amplitude of the applied force  $f_0$ . Mapping these values through a series of  
239 experiments leads to a surface that correlates frequency, amplitude of response and amplitude  
240 of applied force. The surface can be represented as contours that relate frequency and  
241 amplitude of response at constant applied force. In this representation, resonance frequencies  
242 are identified as points of minimum required force, i.e. as the valley of this surface. The  
243 results in Fig. 7(a) show the natural frequencies as the black dotted line. The corresponding  
244 backbone curve presents a sharp change in slope as the frequency leaves the bandgap (shaded  
245 blue region), which presumably indicates a transition in dynamic behavior. In addition,  
246 we record the dynamic deformed shape for excitation at the backbone frequencies. The  
247 measurements are conducted by repeating LDV recordings at each spinner location and then  
248 combining the corresponding amplitude and phase to obtain each of the curves shown in

249 Fig. 7(b). For these, the LDV head is manually moved between locations and the data  
 250 acquisition device is programmed to synchronize the measurements by starting them always  
 251 at the same time interval after the excitation signal is triggered. The figure presents the  
 252 change in the dynamic deformed shapes as a function of total amplitude  $A = |\boldsymbol{\theta}|_2$ , which  
 253 clearly illustrates how the lattice exhibits the predicted change in the linear-regime TP  
 254 mode, and documents its transition from being localized at small amplitudes, to bulk mode  
 255 for higher values of  $A$ . As in the analytical results, the amplitude of motion at spinner  
 256  $n = 1$  is negligible in the linear regime, but grows for increasing nonlinearities (Fig. 7(c)).  
 257 Evidence of a transition, although not as sharp as the one predicted by the theoretical model  
 258 (in Fig. 4), is marked by the vertical solid red line at  $A = 0.08$  rad. We note that Fig. 7(a)  
 259 differs slightly from its analytical counterpart in Fig. 4(b), possibly due to the presence of  
 260 dissipation in the physical system. Evidence of dissipation can be observed in the spatially  
 261 decaying amplitude from the interface in Fig. 7(a), and in the significantly lower  $Q$ -factors  
 262 observed for the experimental lattice in the linear frequency response function of Fig. 6. Also,  
 263 dissipation could contribute to the discrepancy between 4(c) and 7(c). While we believe  
 264 that the effect of dissipation is important and could affect the robustness of TP modes, we  
 265 do not specifically investigate it in this work, and we limit to identifying it as the object of  
 266 future studies.

267 An alternative visualization of the transition is obtained by recording the motion of the  
 268 spinners through a high speed camera. The experiments are conducted by repeating the  
 269 measurements over 15 separate portions of the lattice, as the entire length exceeds the  
 270 aperture of the camera. Measurements are phase-matched and stitched to obtain a single  
 271 recording for an assigned amplitude of motion, snapshots of which for 3 values of amplitude  
 272  $A$  are shown in Fig. 8. As the angular rotation of the spinners in all cases remain relatively  
 273 hard to observe from the pictures, circles of radius proportional to the amplitude of motion  
 274 are superimposed to each spinner to facilitate visualization and to better appreciate the  
 275 extent of the penetration of the mode into the bulk. Such penetration is very limited for low  
 276 amplitudes Fig. 8(a), as the mode is strongly localized at the interface, and progressively  
 277 increases for higher values of amplitude to eventually reach the end of the chain in the case  
 278 shown in Fig. 8(c). Also for visualization purposes, the interior of the circles indicating

279 amplitude is colored to indicate the instantaneous phase of each spinner measured as the  
280 argument of the complex number  $\theta_n e^{j\omega t}$ , where values according to a color scheme varying  
281 from cyan for the lowest values to magenta for the highest ones. A small white circle is also  
282 added to the perimeter of the circles to aid visualization.

#### 283 IV. CONCLUSIONS

284 The paper investigates the occurrence of topologically protected interface modes produced  
285 by broken spatial inversion symmetry. Experimental observations are conducted on a one  
286 dimensional dimer chain consisting of spinners coupled through permanent magnets. Spa-  
287 tial modulation of the interaction strength relies on setting the distance between magnets of  
288 neighboring spinners. Guided by a simplified analytical model, dynamic measurements high-  
289 light the presence of frequency bandgaps and of a TP mode whose frequency lies inside the  
290 bandgap. The experiments also probe the behavior of the chain when nonlinearities affect  
291 lattice interactions. A softening-type nonlinearity cause the frequency of the topologically  
292 protected modes to progressively merge with the linear bulk bands, causing an interface-to-  
293 bulk transition of the corresponding mode. Such transition is first predicted by the analytical  
294 model, and then confirmed by the measured response of the chain. Laser vibrometry and  
295 full field optical capture of the dynamic deformed configurations of the lattice are employed  
296 to quantify and characterize the interface localization of the topologically protected modes,  
297 and their extinction as the amplitude of motion increases. A transition amplitude is pre-  
298 dicted numerically and also observed experimentally, with a good level of agreement. The  
299 study paves a path towards the understanding of the robustness of topologically protected  
300 modes and lack thereof in the presence of the type of nonlinearities investigated as part of  
301 this study. The results also suggest a potential mechanism for the control of localization and  
302 the transition to bulk propagation that exploits topological protection in conjunction with  
303 nonlinear interactions.

304 **ACKNOWLEDGMENTS**

305 The work is supported by the Army Research Office through grant W911NF-18-1-0036,  
306 and by the National Science Foundation through the EFRI 1741685 grant. The authors want  
307 to acknowledge Camille and Emil Prodan for sharing the idea of employing spinners as part  
308 of an effective experimental framework.

---

309 \* Corresponding author: ruzzene@gatech.edu

310 <sup>1</sup> C. L. Kane and E. J. Mele, Phys. Rev. Lett. **95**, 146802 (2005).

311 <sup>2</sup> C. L. Kane and E. J. Mele, Phys. Rev. Lett. **95**, 226801 (2005).

312 <sup>3</sup> C. Brendel, V. Peano, O. Painter, and F. Marquardt, Phys. Rev. B **97**, 020102 (2018).

313 <sup>4</sup> J. Noh, W. A. Benalcazar, S. Huang, M. J. Collins, K. P. Chen, T. L. Hughes, and M. C.  
314 Rechtsman, Nature Photonics **4**, 408 (2018).

315 <sup>5</sup> X. Ni, D. Purtseladze, D. A. Smirnova, A. Slobozhanyuk, A. Alù, and A. B. Khanikaev, Science  
316 Advances **4**, 8802 (2018).

317 <sup>6</sup> R. K. Pal and M. Ruzzene, New Journal of Physics **19**, 025001 (2017).

318 <sup>7</sup> J. Vila, R. K. Pal, and M. Ruzzene, Phys. Rev. B **96**, 134307 (2017).

319 <sup>8</sup> D. Banerjee, A. Souslov, A. G. Abanov, and V. Vitelli, Nature Communications **8**, 1573 (2017).

320 <sup>9</sup> F. Ruesink, J. P. Mathew, M.-A. Miri, A. Alù, and E. Verhagen, Nature Communications **9**,  
321 1798 (2018).

322 <sup>10</sup> N. P. Mitchell, L. M. Nash, and W. T. M. Irvine, Phys. Rev. B **97**, 100302 (2018).

323 <sup>11</sup> A. Souslov, B. C. van Zuiden, D. Bartolo, and V. Vitelli, Nature Physics **13**, 1091 (2017).

324 <sup>12</sup> Y. Hatsugai, Journal of Physics: Condensed Matter **9**, 2507 (1997).

325 <sup>13</sup> R. K. Pal, M. Schaeffer, and M. Ruzzene, Journal of Applied Physics **119**, 084305 (2016).

326 <sup>14</sup> S. Wu, V. Fatemi, Q. D. Gibson, K. Watanabe, T. Taniguchi, R. J. Cava, and P. Jarillo-Herrero,  
327 Science **359**, 76 (2018).

328 <sup>15</sup> Y. Hadad, A. B. Khanikaev, and A. Alù, Phys. Rev. B **93**, 155112 (2016).

329 <sup>16</sup> R. K. Pal, J. Vila, M. Leamy, and M. Ruzzene, Phys. Rev. E **97**, 032209 (2018).

- 330 <sup>17</sup> J. Vila, R. K. Pal, M. Ruzzene, and G. Trainiti, *Journal of Sound and Vibration* **406**, 363  
331 (2017).
- 332 <sup>18</sup> B. Luo, S. Gao, J. Liu, Y. Mao, Y. Li, and X. Liu, *AIP Advances* **8**, 015113 (2018).
- 333 <sup>19</sup> K. J. Moore, J. Bunyan, S. Tawfick, O. V. Gendelman, S. Li, M. Leamy, and A. F. Vakakis,  
334 *Phys. Rev. E* **97**, 012219 (2018).
- 335 <sup>20</sup> A. Kumar, V. Kumar, A. Nautiyal, K. S. Singh, and S. Ojha, *Optik - International Journal for*  
336 *Light and Electron Optics* **145**, 473 (2017).
- 337 <sup>21</sup> J. R. Raney, N. Nadkarni, C. Daraio, D. M. Kochmann, J. A. Lewis, and K. Bertoldi, *Proceed-*  
338 *ings of the National Academy of Sciences* **113**, 9722 (2016).
- 339 <sup>22</sup> M. J. Leamy, R. K. Narisetti, and M. Ruzzene, *Journal of Vibration and Acoustics-Transactions*  
340 *of the Asme* **132** (2010).
- 341 <sup>23</sup> F. Romeo and M. Ruzzene, eds., *Wave Propagation in Linear and Nonlinear Periodic Media*  
342 (Springer, 2012).
- 343 <sup>24</sup> K. Qian, D. J. Apigo, C. Prodan, Y. Barlas, and E. Prodan, *arXiv* **1803.08781v2** (2018).
- 344 <sup>25</sup> J. Zak, *Phys. Rev. Lett.* **62**, 2747 (1989).
- 345 <sup>26</sup> X. Zhou, Y. Wang, D. Leykam, and Y. D. Chong, *New Journal of Physics* **19**, 095002 (2017).
- 346 <sup>27</sup> M. Xiao, G. Ma, Z. Yang, P. Sheng, Z. Zhang, and C. Chan, *Nature Physics* **11**, 240 (2015).
- 347 <sup>28</sup> L. Azrar, R. Benamar, and M. Potier-Ferry, *Journal of Sound and Vibration* **220**, 695 (1999).
- 348 <sup>29</sup> “See supplemental material at xxxx for videos of experimental results,”.
- 349 <sup>30</sup> A. J. Petruska and J. J. Abbott, *IEEE Transactions on Magnetics* **49**, 811 (2013).
- 350 <sup>31</sup> A. Nayfeh and D. Mook, *Nonlinear Oscillations* (Wiley Interscience, 1993).

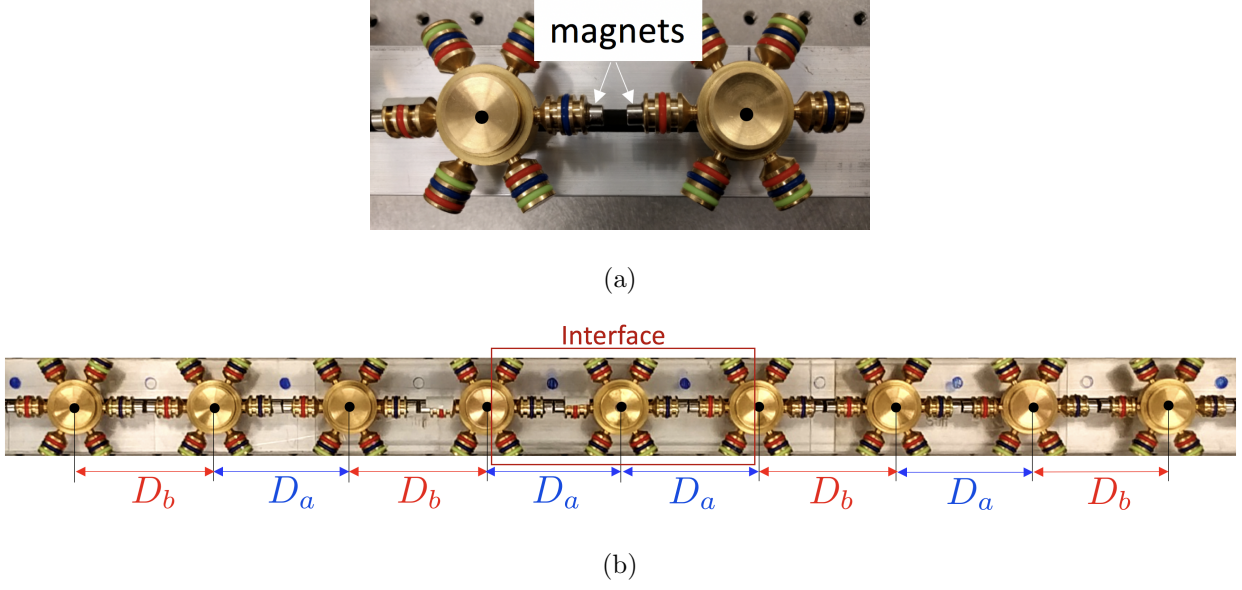


FIG. 1: One-dimensional spinner lattice. (a) Detail of two interacting spinners, and (b) diatomic chain with interface generated through spatial inversion symmetry (SIS).

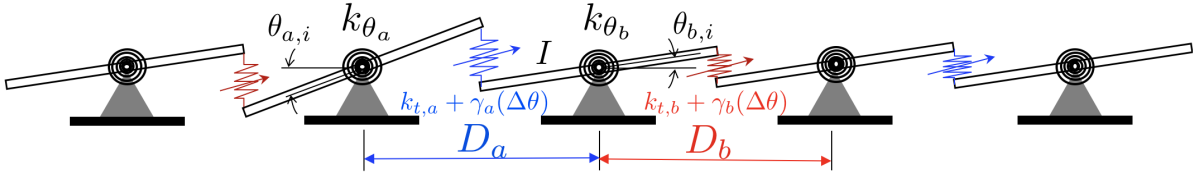


FIG. 2: Schematic of analytical model with key physical parameters.

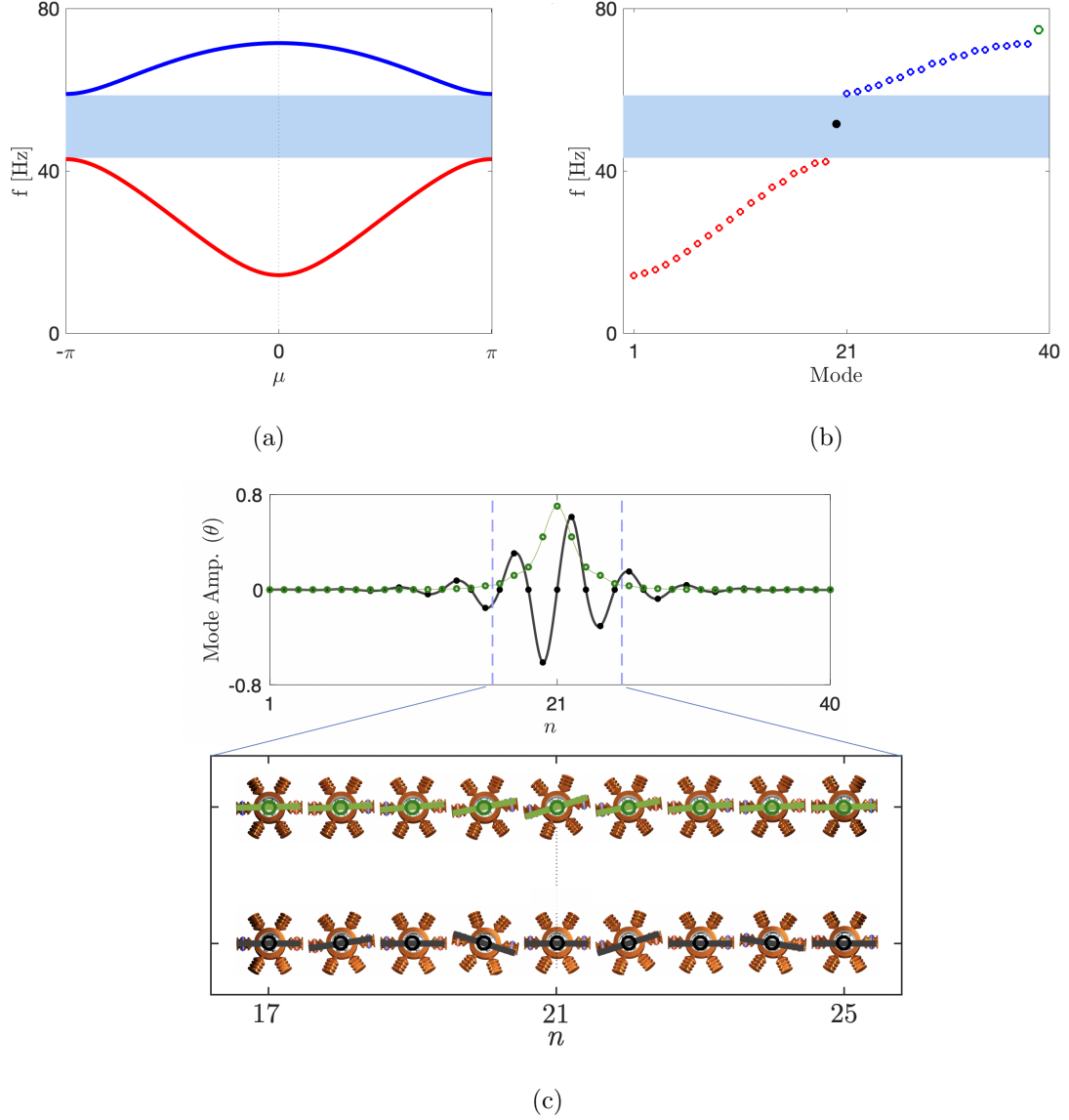


FIG. 3: (a) Linear dispersion diagram for the periodic lattices. (b) Eigenvalues for a 20+20 spinners lattice with the non-trivial interface showing the existence of two interface modes: one populates the bandgap and is topologically protected (black solid dot), a second interface mode appears above the second branch (green circle). (c) Corresponding eigenvectors illustrating the symmetric (even) and antisymmetric (odd) spatial distribution of the interface modes. The TP mode corresponds to the thick black line with solid dots, while the other interface mode is denoted by the thin green line and superimposed circles.

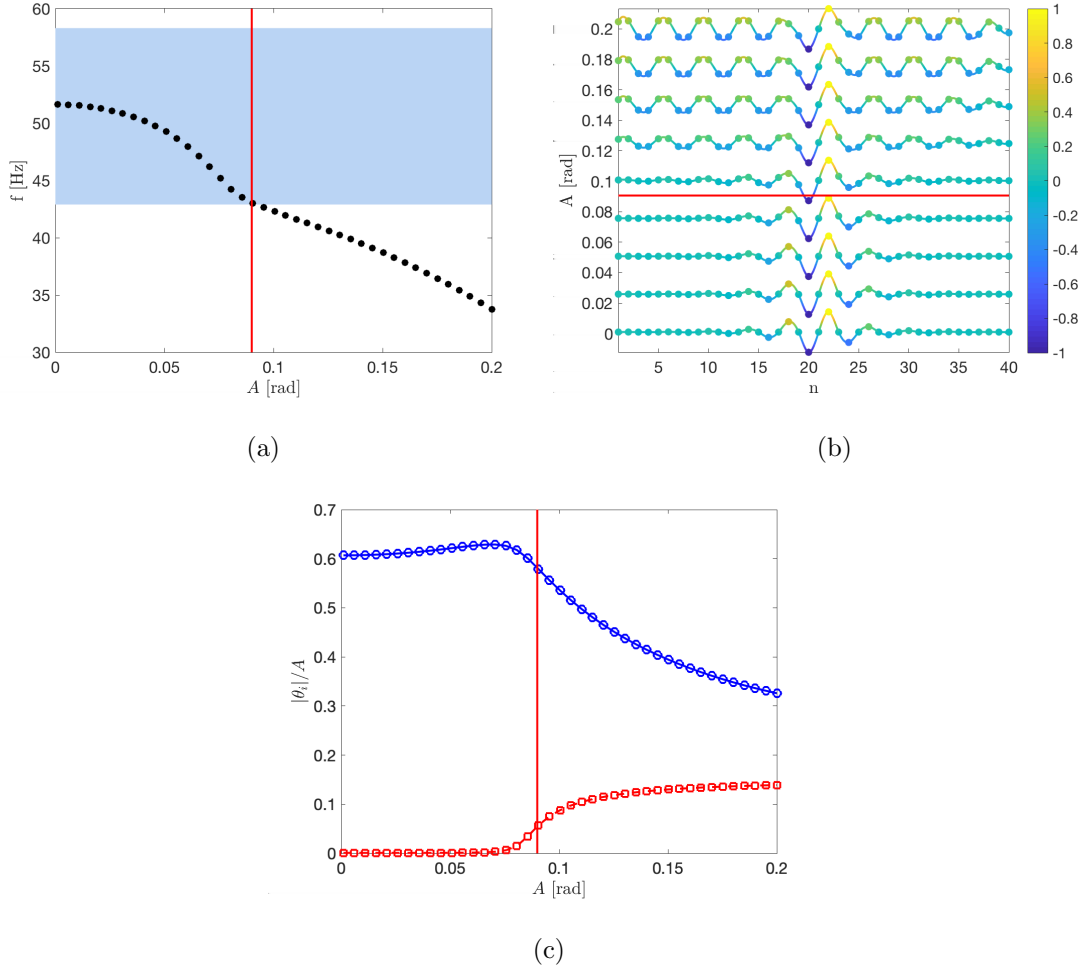


FIG. 4: Effects of nonlinearities on the odd TP mode. (a) Variation of the eigenvalue versus amplitude (black dots); shaded blue area outlines the linear bandgap, while the vertical solid red line marks the amplitude corresponding to the interface-to-bulk transition at  $A \approx 0.09$  rad. (b) Variation of eigenmodes in terms of amplitude (colorbar is associated to the normalized magnitude of each mode). (c) Variation of normalized magnitudes at locations  $n = 1$  (red line with squares) and  $n = 22$  (blue line with blue circles) and transition amplitude (solid red line).

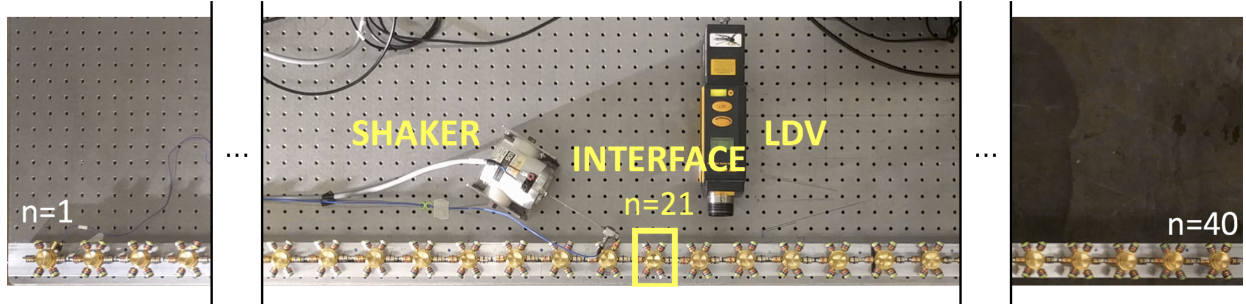


FIG. 5: Physical 40 spinner system mounted on a beam. Distances  $D_a = 7$  mm,  $D_b = 6$  mm are denoted by an empty and a full blue circle respectively (rubber band colors indicate magnets polarity). This is the setup when motion is imposed to spinner 20.

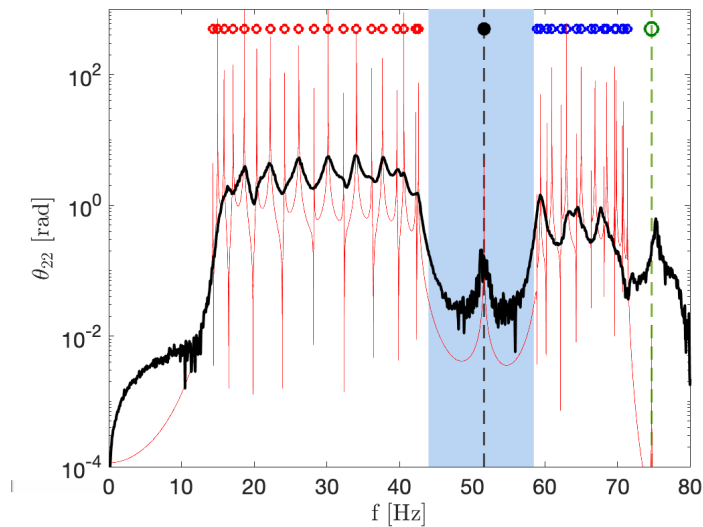
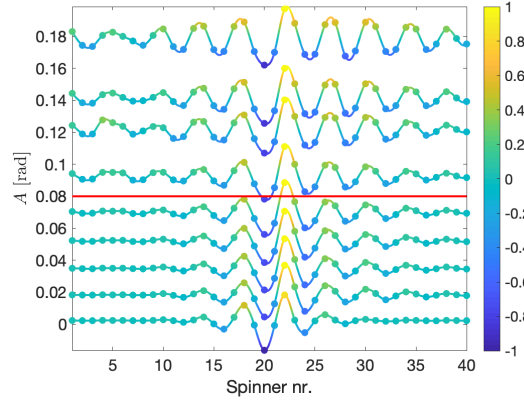
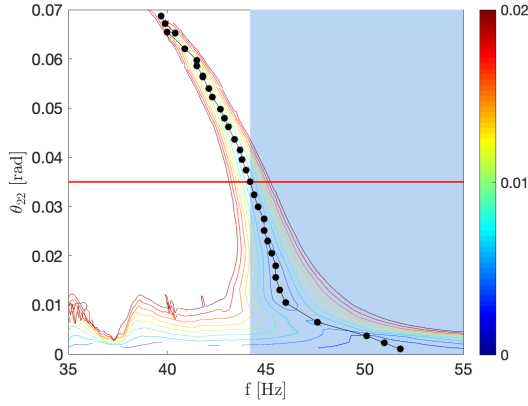


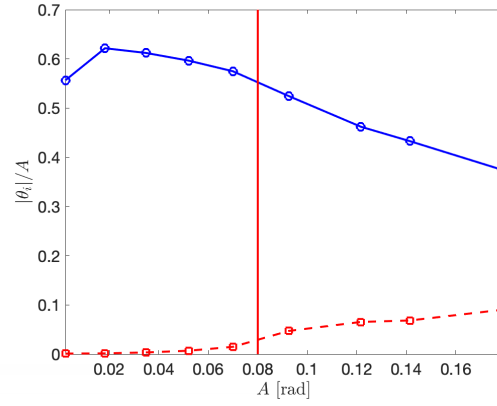
FIG. 6: Experimental frequency response at spinner  $n = 22$  in the *linear regime* for white noise excitation at  $n = 20$ . For reference, the theoretical predictions are reported in the thin red line, along with the theoretical eigenvalues (red and blue circles) and the frequency corresponding to the interface modes (TP mode: black dot, interface mode: green circle and vertical dashed lines). The shaded blue region denotes the analytical linear bandgap.



(a)

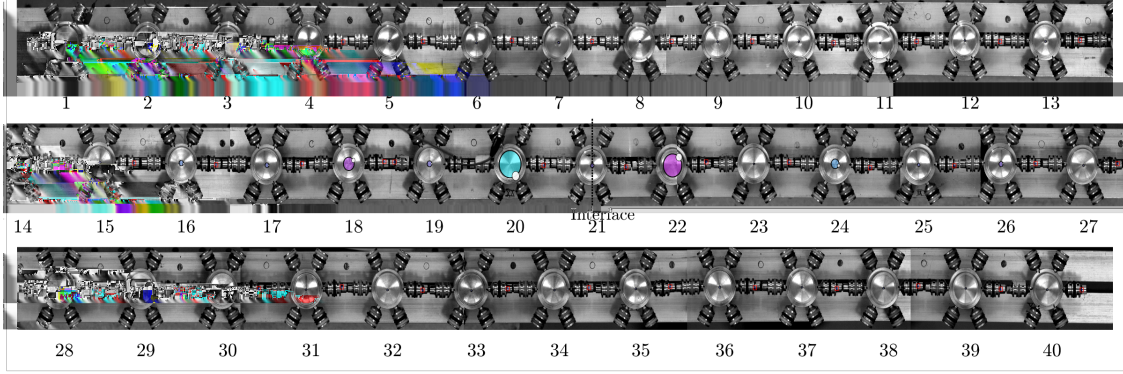


(b)

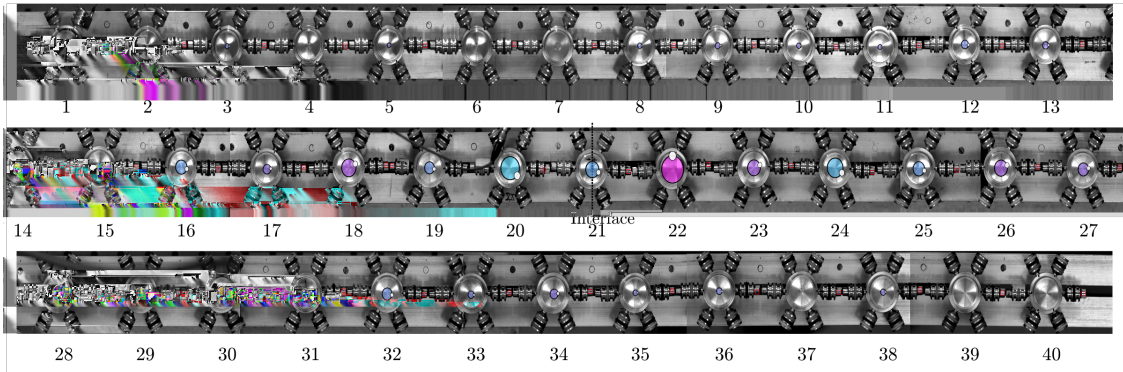


(c)

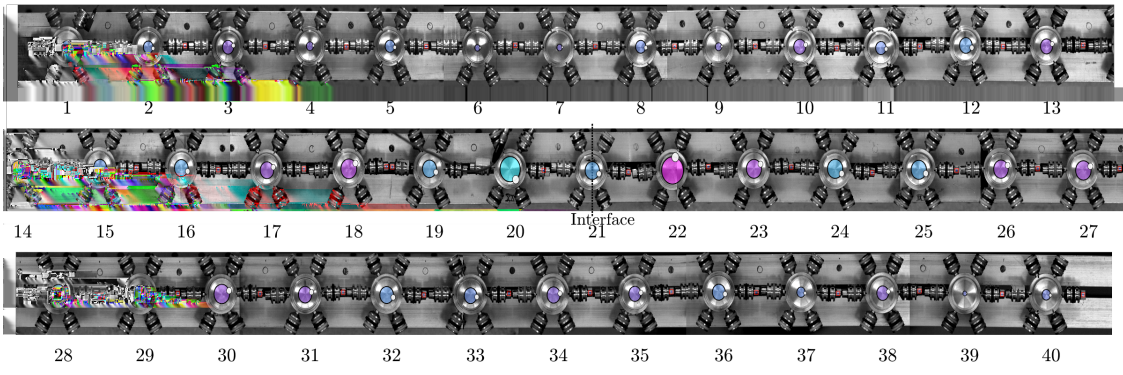
FIG. 7: Experimentally observed effects of nonlinearities on the odd TP mode. (a) Amplitude  $|\Theta_{22}|$  versus frequency relation for nonlinear normal modes. Shaded blue area outlines the linear bandgap, while the horizontal solid red line marks the amplitude corresponding to the interface-to-bulk transition at  $|\theta_{22}| \approx 0.035$  rad. The contours represent the frequency-response correlation for oscillations excited at constant force amplitude. (b) Variation of steady-state dynamic deformed shapes in terms of total amplitude  $A$  (the colorbar denotes the magnitude of the applied force). The transition occurs at amplitude  $A \approx 0.08$  rad. (c) Variation of normalized magnitudes at locations  $n = 1$  (dashed red line and squares) and  $n = 22$  (thick blue line and circles) and transition amplitude (solid red line).



(a)



(b)



(c)

FIG. 8: Experimentally measured snapshots of the chain motion for increasing values of amplitude: (a) low amplitude  $A = 0.002$  rad; (b) medium amplitude  $A = 0.070$  rad, and (c) high amplitude  $A = 0.179$  rad. Circles of radius proportional to the normalized angular motion of each spinner are superimposed to the picture to aid visualization.

351 **Appendix A: Model of magnetic interaction**

352 The magnetic force is evaluated by computing the interaction between magnetically rigid  
 353 dipole moments  $\mathbf{m}_a$  and  $\mathbf{m}_b$ , which is given by<sup>30</sup>:

$$\mathbf{f}_{ba} = -\frac{3\mu_0}{4\pi d^5}(\mathbf{d}(\mathbf{m}_a \cdot \mathbf{m}_b) + \mathbf{m}_a(\mathbf{d} \cdot \mathbf{m}_b) + \mathbf{m}_b(\mathbf{d} \cdot \mathbf{m}_a) - \frac{5\mathbf{d}}{d^2}(\mathbf{d} \cdot \mathbf{m}_a)(\mathbf{d} \cdot \mathbf{m}_b)) \quad (\text{A.1})$$

354 where  $\mathbf{f}_{ba}$  is the force that magnetic dipole  $\mathbf{m}_b$  exerts over dipole  $\mathbf{m}_a$ ,  $\mathbf{d}$  is the vector between  
 355 magnet centers ( $d = |\mathbf{d}|$ ) and  $\mu_0$  is the value of the vacuum magnetic permeability. Here,  
 356 the magnitude of the magnetic dipoles are considered equal, i.e.  $|\mathbf{m}_a| = |\mathbf{m}_b| = m$ .

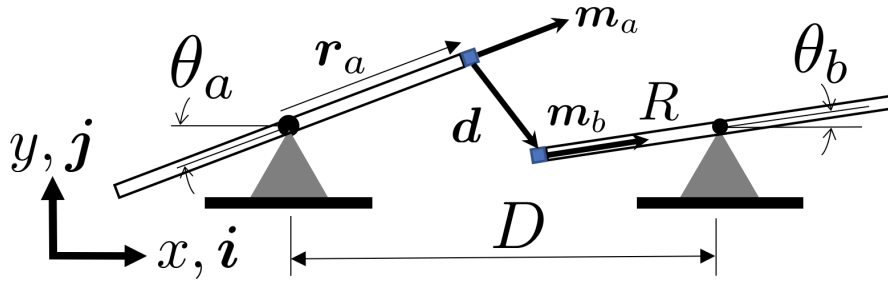


FIG. A.1: Sketch of two spinners interacting through permanent magnets: degrees of freedom and relevant parameters.

357 According to the schematic of Fig. A.1, the dipole moments are expressed as

$$\mathbf{m}_a = m(\mathbf{i} \cos \theta_a + \mathbf{j} \sin \theta_a), \quad \mathbf{m}_b = m(\mathbf{i} \cos \theta_b + \mathbf{j} \sin \theta_b),$$

358 while the relative distance vector is

$$\mathbf{d} = \mathbf{i} [D - R(\cos \theta_a + \cos \theta_b)] - \mathbf{j} [R(\sin \theta_a + \sin \theta_b)].$$

359 The interaction force can be conveniently resolved in terms of the unit vector pair  $\mathbf{i}, \mathbf{j}$ ,  
 360 i.e.  $\mathbf{f}_{ab} = f_x \mathbf{i} + f_y \mathbf{j}$ , where the two force components can be approximated through a Taylor  
 361 series expansion about the equilibrium position  $\theta_a, \theta_b \approx 0$ . Truncation to the first order  
 362 gives:

$$\begin{aligned} f_x &= \frac{3m^2\mu_0}{2\pi(D-2R)^4} + O(\theta_a^2, \theta_b^2, \theta_a\theta_b), \\ f_y &= -\frac{3m^2\mu_0(D+2R)}{4\pi(D-2R)^5}(\theta_a + \theta_b) + O(\theta_a^2, \theta_b^2, \theta_a\theta_b). \end{aligned} \quad (\text{A.2})$$

363 The horizontal component is constant in linear regime, while the vertical one is proportional  
364 to the angle sum  $(\theta_a + \theta_b)$ , i.e. to the relative displacement between neighboring magnets in  
365 the vertical direction. The equation of motion for spinner ( $a$ ) is simply  $I\ddot{\theta}_a - \mathcal{T}_{ba}(\theta_a, \theta_b) = 0$ ,  
366 and includes the moment corresponding to the interaction force, which is given by  $\mathcal{T}_{ba} =$   
367  $|\mathbf{r}_a \times \mathbf{F}_{ba}|$ , where  $\mathbf{r}_a = R(\mathbf{i} \cos \theta_a + \mathbf{j} \sin \theta_a)$  is the vector that goes from center of spinner  $a$   
368 to the center of the magnet  $\mathbf{m}_a$ . This gives:

$$\begin{aligned} \mathcal{T}_{ba} = & -\frac{3m^2\mu_0R}{4\pi(D-2R)^5}(2(D-2R)\theta_a \\ & + (D+2R)(\theta_b + \theta_a)) + O(\theta_a^3, \theta_a^2\theta_b, \theta_a\theta_b^2, \theta_b^3) \end{aligned} \quad (\text{A.3})$$

369 The expression above include one term depending solely on  $\theta_a$  and another that is directly  
370 proportional to  $(\theta_a + \theta_b)$ . The first term is analogous to the torque exerted by a spring  
371 connected to the ground, and is the result of the horizontal attractive force component  
372 between the magnets. The second term is proportional to the relative angular motion of  
373 neighboring spinners and is associated with the vertical component of the interaction force.

374 In order to account for nonlinearities in moderate rotation regimes, we extend the Taylor  
375 series expansion of the torque  $\mathcal{T}_{ba}$  up to order 3, which gives:

$$\begin{aligned} \mathcal{T}_{ba} = & -\frac{3m^2\mu_0R}{4\pi(D-2R)^5} \left( 2(D-2R)\theta_a + (D+2R)(\theta_b + \theta_a) \right) \\ & + \frac{m^2\mu_0R}{8\pi(D-2R)^7} \left( (3D^3 + 12D^2R + 3DR^2 + 16R^3)(\theta_b + \theta_a)^3 \right. \\ & + (9D^3 + 4D^2R - 46DR^2)\theta_a^3 + (3D^3 - 6D^2R + 42DR^2 - 96R^3)\theta_a^2\theta_b + (6DR^2)\theta_a\theta_b^2 \\ & \left. + (-2D^3 + 10D^2R + 2DR^2 - 32R^3)\theta_b^3 \right) + O(\theta_a^4, \dots). \end{aligned} \quad (\text{A.4})$$

376 The nonlinear part of the torque includes five terms whose importance can be evaluated  
377 for the considered values of  $D = 70.9$  mm and  $R = 32.45$  mm, which gives  $R/D \approx 0.46$ .  
378 Numerical estimation of the coefficients reveals that the term for  $(\theta_b + \theta_a)^3$  is at least an  
379 order of magnitude larger than all other nonlinear coefficients. Therefore, the torque can be  
380 further approximated as follows:

$$\mathcal{T}_{ba} \approx -k_\theta\theta_a - k_t(\theta_a + \theta_b) - \gamma(\theta_a + \theta_b)^3, \quad (\text{A.5})$$

381 where

$$\begin{aligned}
k_\theta &= \frac{6m^2\mu_0R}{4\pi(D-2R)^5}(D-2R) \\
k_t &= \frac{3m^2\mu_0R}{4\pi(D-2R)^5}(D+2R), \\
\gamma &= -\frac{m^2\mu_0R}{8\pi(D-2R)^7}(3D^3+12D^2R+3DR^2+16R^3).
\end{aligned} \tag{A.6}$$

382 which leads to the following governing equation of motion for the spinner:

$$I\ddot{\theta}_a + k_{\theta,a}\theta_a + k_{t,a}(\theta_a + \theta_b) + \gamma_a(\theta_a + \theta_b)^3 = 0 \tag{A.7}$$

383 The negative sign in the nonlinear coefficient  $\gamma$  in equation (A.6) indicates that the cubic  
384 exponential term has a softening effect on the dynamic behavior of the spinner.

385 Please note that  $k_\theta$  takes two different values in the chain  $k_{\theta,a}$  and  $k_{\theta,b}$  depending if the  
386 distance between spinners is  $D_a$  or  $D_b$  respectively. However, they add up in each spinner,  
387 since there is one spinner to the left and one to the right both contributing with a constant  
388 restoring longitudinal force  $f_l$ . As a result, all of them are the same  $k_{\theta,a}+k_{\theta,b} = k_{\theta,b}+k_{\theta,a} = k_\theta$ ,  
389 except for three spinners: the left boundary  $n = 1$  is  $k_{\theta,b}$ , the right boundary  $n = 40$  is  $k_{\theta,a}$ ,  
390 and the interface  $n = 21$  which is  $2k_{\theta,a}$ . This is taken into account in the analytic calculations.

391 Hence, the motion of regular  $i$ -th unit cell is expressed by Eq. (1) and the motion of the  
392 inverted  $i$ -th unit cell is formulated as

$$\begin{aligned}
I\ddot{\theta}_{b,i} + k_\theta\theta_{b,i} + k_{t,b}(\theta_{a,i} + \theta_{b,i}) + k_{t,a}(\theta_{b,i} + \theta_{a,i-1}) + \gamma_b(\theta_{a,i} + \theta_{b,i})^3 + \gamma_a(\theta_{b,i} + \theta_{a,i-1})^3 &= 0 \\
I\ddot{\theta}_{a,i} + k_\theta\theta_{a,i} + k_{t,a}(\theta_{b,i+1} + \theta_{a,i}) + k_{t,b}(\theta_{a,i} + \theta_{b,i}) + \gamma_a(\theta_{b,i+1} + \theta_{a,i})^3 + \gamma_b(\theta_{a,i} + \theta_{b,i})^3 &= 0
\end{aligned} \tag{A.8}$$

## 393 Appendix B: Experimental evaluation of magnetic interaction coefficients

### 394 1. Linear coefficients

395 The analytical model relies on the experimental estimation of linear and nonlinear co-  
396 efficients  $k_\theta$ ,  $k_t$  and  $\gamma$  as a function of the distance between neighboring magnets faces

397  $d_0 = D - 2R - h_m$ , where  $h_m = 5$  mm is the height of the magnets. To this end, we  
 398 use a 3 spinner system which is tested dynamically. First, low-amplitude (linear) white noise  
 399 excitation is applied to the left spinner  $n = 1$  in Fig. B.1a. The resonant frequencies of the  
 400 resulting 2 degree of freedom system are recorded based on the evaluation of the response  
 401 peaks. Estimation of the linear coefficients is based on the analytical expressions for these  
 402 resonant frequencies, which are:

$$f_{r_{1,2}}^2 = \frac{1}{2\pi} \left( 3k_\theta + 3k_t \pm \sqrt{k_\theta^2 + 2k_\theta k_t + 5k_t^2} \right) / 2I$$

403 from which values of  $k_\theta(d_0)$  and  $k_t(d_0)$  are inferred. Exemplary results are shown in Fig. B.1b,  
 404 while the full set of estimated coefficients are listed in Table B.1.

405 The estimated coefficients are subsequently used to evaluate the attractive horizontal  
 406 component of the force  $f_x(d_0)$ , which is then compared with the data provided by the per-  
 407 manent magnets manufacturer (D4H2 nickel plated neodymium magnets by K&J Magnetics,  
 408 Inc.). The comparison in Fig. B.1c shows a very good agreement and confirms the accuracy  
 409 of the estimated coefficients, which are then used as inputs to the analytical model.

TABLE B.1: Experimental values of constants  $k_\theta$  and  $k_t$  as a function of distance between  
 magnets  $d_0 = D - 2R - h_m$ .

$d_0$ (mm)	1	2	3	4	5	6	7
$k_\theta$ (Nm/rad)	0.194	0.115	0.072	0.056	0.045	0.036	0.028
$k_t$ (Nm/rad)	2.385	1.224	0.720	0.406	0.282	0.178	0.127

## 410 2. Nonlinear coefficients

411 Subsequently, we estimate the nonlinear coefficient  $\gamma$  using the 2-spinner system shown in  
 412 Fig B.2a. In this set-up, the left spinner 1 is forced to oscillate harmonically at a particular  
 413 amplitude and frequency, while spinner 2 is clamped in the  $\theta_2 = 0$  position. We run a set of  
 414 dynamic nonlinear steady-state experiments in which the exerted periodic force is recorded

415 with a load cell (model 208C01 by PCB Piezotronics Inc.) from which the amplitude of its  
 416 first harmonic  $f_0$  is extracted.

417 Since the shaker is controlled in open-loop, we control the amplitude and frequency of the  
 418 harmonic electronic signal sent to the shaker that imposes the motion  $\theta_1 e^{i\omega t}$ , and its velocity  
 419 is measured with the LDV, from which the amplitude of its first harmonic  $\theta_1$  is calculated.  
 420 Then, for each experiment, we get a triplet of values: the amplitude of the response  $\theta_1$ , its  
 421 frequency, and the amplitude of the applied force  $f_0$ . The experiment is repeated over a  
 422 range of imposed amplitudes from 0 to 0.04 rad and frequencies from 30 to 43 Hz. Mapping  
 423 the results produces a surface that correlates frequency, amplitude of response and amplitude  
 424 of applied force. The contours of this surface correlate frequency and amplitude of response  
 425 for constant amplitude of excitation force  $f_0$ .

426 For this range of amplitudes and based on the assumptions described in Appendix A,  
 427 the governing equation of the forced response is equivalent to that of an undamped Duffing  
 428 oscillator,

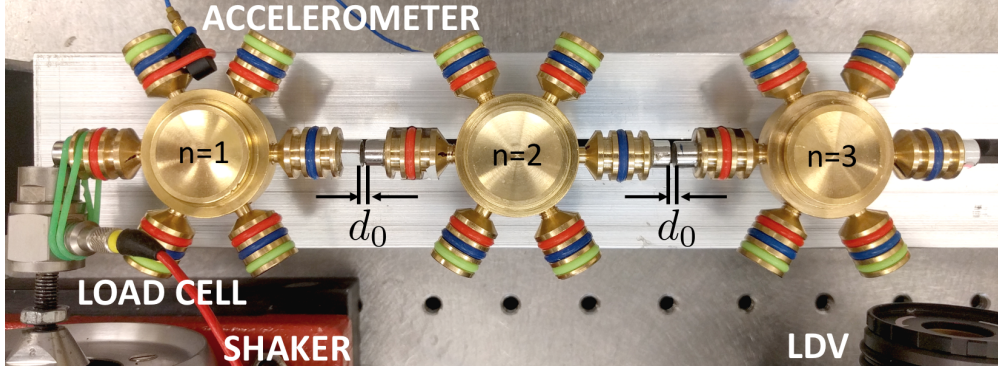
$$I\ddot{\theta}_1 + (k_\theta + k_t)\theta_1 + \gamma\theta_1^3 = f(t) \quad (\text{B.1})$$

429 where  $f(t)$  is the external force.

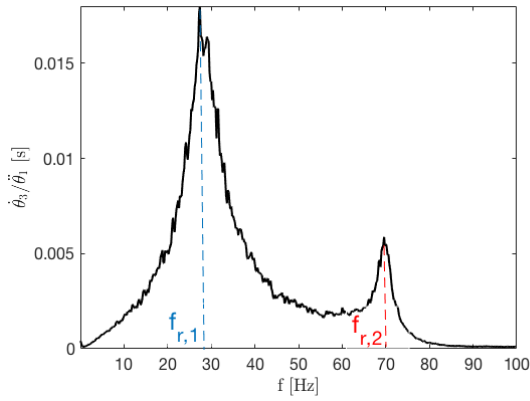
430 The response amplitude for harmonic excitation  $f(t) = f_0 \cos(\omega t)$  can be obtained ana-  
 431 lytically from<sup>31</sup>

$$(I\omega^2 - (k_\theta + k_t) - 3/4\gamma A^2)^2 A^2 = f_0^2 \quad (\text{B.2})$$

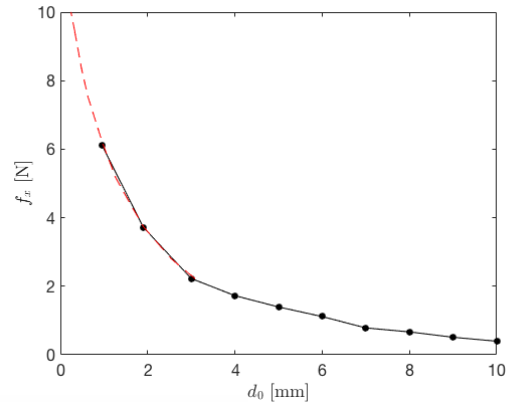
432 where  $A$  is the amplitude of the response in  $\theta_1 e^{i\omega t}$ , with  $A = |\theta_1|$ . By comparing the measured  
 433 response with the analytical predictions according to the expression above, we estimated  
 434 a value for the nonlinear coefficient equal to  $\gamma = -320 \text{ Nm/rad}^3$  for a distance between  
 435 neighboring magnets  $d_0 = 1.2 \text{ mm}$ . The comparison is shown in Fig. B.2d, which illustrates  
 436 the excellent match between analytical predictions (dashed lines) and experimental results  
 437 (solid lines) for the estimated value of  $\gamma$ . In the figure, each color relates amplitude and  
 438 frequency for a different value of excitation force amplitude  $f_0$ . Through the same process,  
 439 we estimate that  $\gamma(d_0 = 1 \text{ mm}) = -366 \text{ Nm/rad}^3$  and  $\gamma(d_0 = 2 \text{ mm}) = -188 \text{ Nm/rad}^3$ .



(a)



(b)

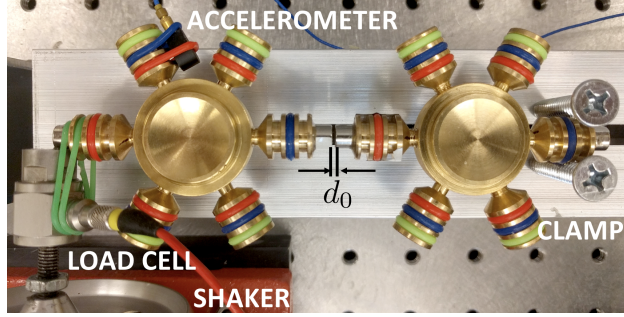


(c)

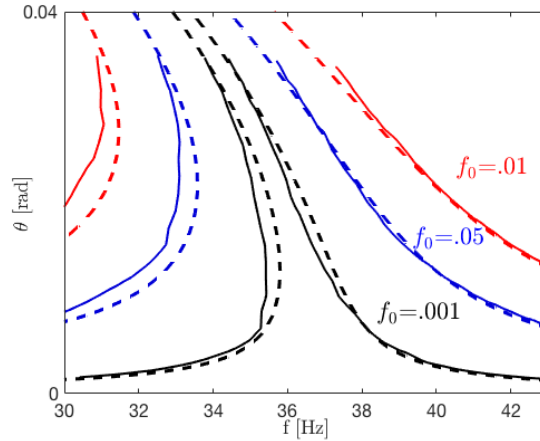
FIG. B.1: (a) Setup for the characterization of linear constants  $k_\theta$  and  $k_t$ . The magnet distance is set at  $d_0 = 1$  mm. (b) Frequency response function of the system showing the occurrence of two resonance frequencies that are related to the constants  $k_\theta$  and  $k_t$  and recorded for their estimation, which is based on repeating the measurements for varying magnets distance  $d_0$ . (c) Comparison of the longitudinal attraction force  $f_x$  evaluated on the basis of the estimated constants (black dots) and corresponding force provided in the technical specifications from the retailer (red dashed line).

#### 440 Appendix C: Experimental setup and methods

441 The complete spinner chain is bolted to a straight slotted beam, which allows adjusting  
 442 the inter-magnetic distances as needed by the experiments. The spinner radius is  $R = 32.45$



(a)



(b)

FIG. B.2: (a) Setup for measuring the nonlinear forced response in a 1 dof system. Harmonic motion is imposed and the exerted force is measured for different amplitudes and frequencies. (b) Then the coefficient  $\gamma$  is fine-tuned so that the analytical solution of the Duffing oscillator (dashed) matches the experimental results (solid) for different amplitudes of the force  $f_0$ .

443 mm, which leads to a rotary inertia value of  $I = 37.2 \text{ Kg mm}^2$  including the magnets. We  
 444 calculate the inertia using meticulous measurements of the volumes and masses of all the  
 445 parts conforming each spinner. We measured all the geometry parameters of the spinners:  
 446 the main body, the pegs, the bearings and the bearing balls. From a detailed CAD model,  
 447 a view of which is provided in Fig. C.1, we calculated the volumetric inertias ( $m^5$ ) of three  
 448 different parts: the spinner body and pegs, the bearing outer cylinder, and the bearing balls.

449 Those were obtained by numerical integration about the axis of gyration  $I_V = \sum (r_i^2 \delta V_i)$ ,  
 450 where  $r_i$  is the distance between the center of the  $i$ -th differential volume  $\delta V_i$  and the axis of  
 451 gyration. We also calculated the volumes and weighted the parts separately. Assuming that  
 452 the materials are homogeneous, we estimate the density  $\rho_m$  of each part  $m$ . We calculate the  
 453 mass inertia by multiplying the volumetric inertia by the density of each part  $I = \sum I_{V,m} \rho_m$ .  
 454 The bearing balls contribute half because its motion is half of the rest of the spinner. We  
 455 neglected the spinning of the bearing balls in the motion. The magnets, which are 5 mm tall  
 456 and 6.35 mm diameter, are placed at distances  $d_{0,a} = 1$  mm and  $d_{0,b} = 2$  mm apart. The  
 457 corresponding distances between the centers of the spinners are respectively  $D_a = 70.9$  mm  
 458 and  $D_b = 71.9$  mm. Figure C.2 shows a top view of the experimentally tested 40 spinner  
 459 chain.

460 In the experiments we impose harmonic motion to the spinner at the left boundary  $\theta_1$   
 461 or the spinner next to the interface  $\theta_{20}$  depending on each experiment goal, with a shaker  
 462 controlled in open loop. The shaker, a model V201 by LDS LTD., is excited with an electronic  
 463 signal programmed in the PC and sent through the data acquisition system (DAQ), (USB-  
 464 6366 782263-01 by National Instruments TM). We measure the acceleration of the excited  
 465 spinner using the accelerometer (model 352A24 by PCB Piezotronics Inc.) and calculate its  
 466 motion by integration. The motion of the other spinners is calculated from integration of the  
 467 velocities, which in turn are measured by LDV using a PDV-100 scanning head by Polytech  
 468 GmbH. This is a single point LDV, so we repeat the experiments 40 times and move the  
 469 LDV device manually between locations to measure the motion of all the spinners. The  
 470 DAQ is used to trigger the excitations and measurements always with the same time interval  
 471 between them, which ensures that the steady-state is reached and that phase is synchronized  
 472 between experiments.

473 The signal imposed to the shaker is either white noise over the frequency range of interest  
 474 ( $0 - 80$  Hz) to provide the response of the system in the frequency domain, or harmonic for  
 475 steady-state measurements. The signal is properly amplified to obtain the targeted ampli-  
 476 tudes of displacement in the shaker. These amplitudes are monotonically but not propor-  
 477 tionally related to the amplitude of the electronic signal that excites the shaker. Therefore,  
 478 we can increase and decrease the amplitude of motion  $\theta_{20}$  imposed to spinner  $n = 20$  without

479 knowing its exact value *a priori*. The exact value of the motion is calculated *a posteriori*  
480 from the accelerometer measurements. At the same time, the force at the shaker tip is mea-  
481 sured using a force transducer model 208C01 by PCB Piezotronics Inc. These signals are  
482 amplified for acquisition using a signal conditioner model 482A21 by PCB Piezotronics Inc.  
483 Finally, videos of the motion in the steady-state nonlinear experiments are recorded using  
484 a high speed camera model 675K-M1 by Photron USA, Inc. placed right above the spinners  
485 system (not shown in the figure). Due to the length of the chain, all the 40 spinners do  
486 not fit in the camera frame if we want to maintain a good level of resolution. Therefore,  
487 we use 15 different camera positions, recording 2 or 3 spinners at a time. We use the DAQ  
488 to control and coordinate the excitation, the measurements and the camera trigger, so that  
489 we ensure phase synchronization between the videos. These were later post-processed and  
490 stitched together using Matlab software.

491 The snapshots of the deformed configurations of the chain shown in Fig. 8 are extracted  
492 from the movies provided as supplementary material<sup>29</sup>. In the snapshots and in the movies,  
493 visualization of the angular rotation of the spinners is aided by superimposing to each spin-  
494 ner a colored circle of radius proportional to the amplitude of motion. Also, the rotation  
495 angle is extracted from the video by employing in-house Digital Image Correlation software.  
496 The lengthwise variation of the rotation angle of the spinners is shown in the graphs accom-  
497 panying each of the response movie, which helps visualizing the spatial extent of motion and  
498 differentiating localized modes versus bulk-propagating modes.



FIG. C.1: Solid model of a single spinner showing details of its construction.

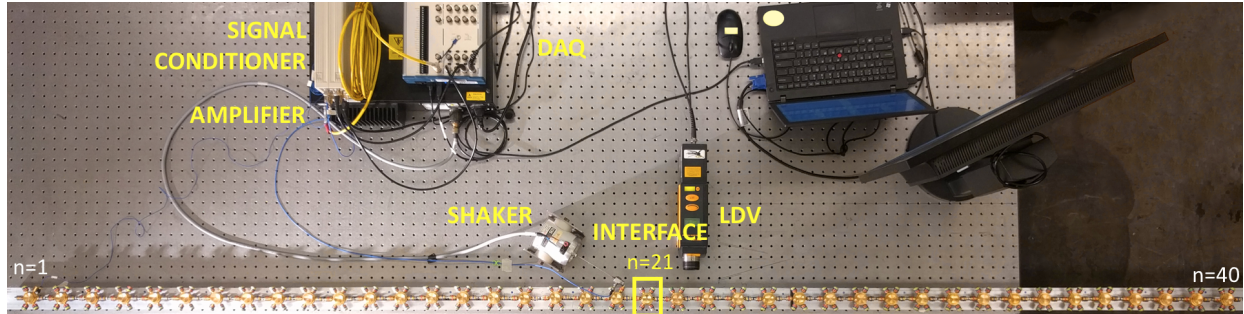


FIG. C.2: Physical 40 spinner system mounted on a beam. Distances between magnets are  $d_{0,a} = 1$  mm and  $d_{0,2} = 2$  mm. Transducers and data acquisition devices are also shown.

499 In detail, we provide the following movies as supplementary material<sup>29</sup>:

500 SM1 Description of the experimental set-up and animation explaining the spinner lattice  
 501 visualization in Fig. 8. The experiments are conducted by repeating the measurements  
 502 over 15 separate portions of the lattice, as the entire length exceeds the aperture of the  
 503 camera. Upon recording, the measurements are phase-matched and stitched to obtain  
 504 a single recording for an assigned amplitude of motion.

505 SM2 Experimental results recorded for low amplitude excitation, and corresponding to the  
 506 still picture of Fig. 8(a). The recorded video data are used to extract angular informa-  
 507 tion about the rotation of the spinners, which is plotted as a function of the spinner  
 508 number in the bottom graph. This visualization helps observing the localized nature  
 509 of the dynamic deformed lattice response at low amplitude excitation corresponding  
 510 to the TP mode.

511 SM3 Experimental results recorded for medium amplitude excitation, and corresponding to  
 512 the still picture in Fig. 8(b). The plot of the angular motion of the spinners shows the  
 513 increase in penetration of the dynamic response which extends away from the interface  
 514 as amplitude increases.

515 SM4 Experimental results recorded for high amplitude excitation, and corresponding to the  
 516 still picture of Fig. 8(c). The plot of the spinners' rotation clearly shows that the mode  
 517 now extends to the entire length of the chain.